Mon. Not. R. Astron. Soc. **000**, 1-11 (2008) Printed 9. November 2010 (MN LATEX style file v2.2)

A study of relative velocity statistics in Lagrangian perturbation theory with PINOCCHIO

Lavinia Heisenberg⋆[1,2], Björn Malte Schäfer[3] and Matthias Bartelmann[2]
[1] *Université de Genève, Département de Physique Théorique, 24, quai E. Ansermet, 1211 Genève, Switzerland*
[2] *Institut für theoretische Astrophysik, Zentrum für Astronomie, Universität Heidelberg, Albert-Ueberle-Straße 2, 69120 Heidelberg, Germany*
[3] *Astronomisches Recheninstitut, Zentrum für Astronomie, Universität Heidelberg, Mönchhofstraße 12, 69120 Heidelberg, Germany*

9. November 2010

ABSTRACT
Subject of this paper is a careful and detailed analysis of the PINOCCHIO algorithm for studying the relative velocity statistics of merging haloes in Lagrangian perturbation theory. Given a cosmological background model, a power spectrum of fluctuations as well as a Gaussian linear density contrast field $\delta_{\rm l}$ is generated on a cubic grid, which is then smoothed repeatedly with Gaussian filters. For each Lagrangian particle at position $\boldsymbol{q}$ and each smoothing radius R, the collapse time, the velocities and ellipsoidal truncation are computed using Lagrangian Perturbation Theory. The collapsed medium is then fragmented into isolated objects by an algorithm designed to mimic the accretion and merger events of hierarchical collapse. Directly after the fragmentation process the mass function, merger histories of haloes and the statistics of the relative velocities at merging are evaluated. We reimplemented the algorithm in C++ and optimised the construction of halo merging histories. Comparing our results with the output of the Millennium simulation suggests that PINOCCHIO is well suited for studying relative velocities of merging haloes and is able to reproduce the pairwise velocity distribution.

Key words: cosmology: large-scale structure, methods: analytical, numerical

1 INTRODUCTION

To account for structure formation one needs to develop techniques for studying the nonlinear evolution of perturbations. In the strongly nonlinear regime where the perturbation amplitudes exceed unity ($|\delta| \gg 1$), the linear approximation breaks down and has to be replaced by other approaches. To accentuate the need for this, one has to look at the interesting structures in the Universe, like galaxies or clusters of galaxies because they are highly nonlinear. Since every theory of structure formation must be capable of describing the formation and evolution of non-linear objects, the major developments have been done in perturbation theory and numerical simulations. It has been understood that this aim simplifies when formulated in terms of Lagrangian coordinates rather than the standard Eulerian ones, since the latter one relies on physical densities being small (Buchert & Weiss 1993; Buchert 1996). So one assumes that the dynamics of gravitational clustering is described more suitably in terms of the displacement field $\boldsymbol{D}$, which is in the Lagrangian approach the only underlying fundamental field. The decisive difference to the Eulerian approach is that it is not based on the smallness of the density of the inhomogeneities and that one searches for solutions of perturbed trajectories about the linear initial displacement $\boldsymbol{D}^{(1)}$ (Sahni & Coles 1995; Bernardeau et al. 2002). The fundamental point is that a small perturbation of the Lagrangian particle paths carries a large amount of non-linear information about the corresponding Eulerian evolved observables, since the Lagrangian picture is intrinsically non-linear in the density field (Buchert 1993). Lagrangian perturbation theory reaches its limit of applicability when trajectories of particles cross and the mapping from the initial conditions to the evolved density field ceases to be unique.

The cosmological model used is a spatially flat ΛCDM cosmology with Gaussian adiabatic initial perturbations in the cold dark matter (CDM) density field with the following cosmological parameter set $(\Omega_{m0}, \Omega_\Lambda, h, \sigma_8) = (0.25, 0.75, 0.73, 0.9)$, identical to that used in the Millennium simulation, to which we will compare our results. Our computational domain is a cubic box of size 128 Mpc/h with periodic boundary conditions filled with $N^3 = 64^3$ particles.

2 COSMOLOGY

2.1 CDM power spectrum

The linear CDM power spectrum $P(k)$ describes the fluctuation amplitude of the Gaussian initial density field δ, $\langle\delta(\boldsymbol{k})\delta(\boldsymbol{k}')\rangle = (2\pi)^3\delta_D(\boldsymbol{k}+\boldsymbol{k}')P(k)$, and is given by the ansatz

$$P(k) \propto k^{n_s} T^2(k), \qquad (1)$$

⋆ e-mail: lavinia.heisenberg@unige.ch

with the transfer function $T(k)$ which is approximated by (Bardeen et al. 1986),

$$T(q) = \frac{\ln(1+aq)}{aq}\left(1 + bq + (cq)^2 + (dq)^3 + (eq)^4\right)^{-\frac{1}{4}}, \quad (2)$$

with the fitting parameters $a = 2.34$, $b = 3.89$, $c = 16.1$, $d = 5.46$, $e = 6.71$. In the transfer function, the wave number $k = q\Gamma$ enters rescaled by the shape parameter Γ (Sugiyama 1995),

$$\Gamma = \Omega_m h \exp\left(-\Omega_b\left(1 + \frac{\sqrt{2h}}{\Omega_m}\right)\right). \quad (3)$$

For further treatment one introduces the smoothed density field δ_R, which is averaged on the scale R,

$$\delta_R(\boldsymbol{x}) = \int d^3y\, \delta(\boldsymbol{y}) W_R(|\boldsymbol{x}-\boldsymbol{y}|) \quad (4)$$

with the window function $W_R(r)$, satisfying $\int d^3x\ W_R(|\boldsymbol{x}|) = 1$. Working in the Fourier space, one obtains

$$\tilde{\delta}_R(\boldsymbol{k}) = \tilde{\delta}(\boldsymbol{k})\tilde{W}_R(\boldsymbol{k}), \quad (5)$$

and for the smoothed power spectrum

$$P_R(k) = |\tilde{W}_R(k)|^2 P(k). \quad (6)$$

There exist several choices for the window function W_R, apart from the widely used Gaussian window function, a very common one is top-hat filtering, which is given by

$$W_R(|\boldsymbol{x}|) = \frac{3}{4\pi R^3}\Theta(R - |\boldsymbol{x}|), \quad (7)$$

where Θ denotes the Heaviside step function. The Fourier transform for this specific window function is

$$\tilde{W}_R(k) = 3\,\frac{\sin(kR) - kR\cos(kR)}{(kR^3)}. \quad (8)$$

Using the definitions introduced so far, it is now straightforward to calculate the variance $\sigma^2(R) = \langle\delta_r^2(\boldsymbol{x})\rangle$ of the smoothed density field as

$$\sigma^2(R) = \int \frac{d^3k}{(2\pi)^3}\, P_R(k) = \int \frac{d^3k}{(2\pi)^3}\, |\tilde{W}_R(k)|^2 P(k). \quad (9)$$

Including the window function $\tilde{W}_R(k)$ and the power spectrum $P(k)$ in this equation, together with

$$\sigma^2(R = 8\ \mathrm{Mpc}/h) \equiv \sigma_8^2 \quad (10)$$

fixes the normalization.

3 LAGRANGIAN PERTURBATION THEORY

The formation of CDM haloes involves highly non-linear dynamical processes which can only be followed in numerical simulations or by applying perturbative methods. As mentioned in the introduction, one important approach is Lagrangian Perturbation Theory. In order to describe the non-linear dynamical evolution of the particle trajectories up to third order Lagrangian coordinates the following three steps have to be followed:

(i) Description of the mapping from the Eulerian to the Lagrangian coordinates

(ii) Transformation of the Eulerian Fields to Lagrangian coordinates

(iii) Application of perturbation theory to the Lagrangian equations expressed by the displacement up to desired order

The starting point is a pressureless, non-vortical, self-gravitating fluid with Newtonian gravity embedded in an expanding Friedmann-Lemaître Robertson-Walker universe (Buchert 1992). In the Lagrangian framework of fluid dynamics the relation between the Eulerian position $\boldsymbol{x}$ of a mass particle and the initial Lagrangian position $\boldsymbol{q}$ is given by the displacement field (Zel'Dovich 1970):

$$\boldsymbol{x}(\boldsymbol{q}, t) = \boldsymbol{q} + \boldsymbol{D}(\boldsymbol{q}, t), \quad (11)$$

In the Lagrangian space the trajectories of the mass elements are fully described by the dynamical mappings $\boldsymbol{x}(\boldsymbol{q}, t)$, starting from the initial positions $\boldsymbol{q}$.

The above equation implies that there is a one-to-one correspondence between the Langrangian coordinate $\boldsymbol{q}$ and the Eulerian coordinate $\boldsymbol{x}$. This certainly is the case only for a cold non-collisional fluid, at least until the stage of caustic formation. Expressed mathematically, this corresponds to the statement that the functional determinant J of the Jacobian of the mapping relation $\boldsymbol{q} \to \boldsymbol{x}(\boldsymbol{q}, t)$ is non-singular,

$$J(\boldsymbol{q}, t) \equiv \det\left(\frac{\partial \boldsymbol{x}}{\partial \boldsymbol{q}}\right) \neq 0\,, \quad (12)$$

which means that the mapping $\boldsymbol{x}(\boldsymbol{q}, t)$ is invertible to $\boldsymbol{q}(\boldsymbol{x}, t)$. It is evident that many particles coming from very different original positions will tend to arrive at the same Eulerian position during the highly non-linear evolution. As a consequence of that infinite-density regions (caustics) will form in Eulerian space. Hence the mapping from Lagrangian to Eulerian space becomes singular and the density infinite as $\rho \propto J^{-1}$. Since the displacement $\boldsymbol{D}$ fully characterizes the map between the Eulerian and the Lagrangian coordinates, the motion of the fluid elements are completely described in terms of it. One can now express the peculiar velocity, acceleration and density contrast by replacing the displacement field $\boldsymbol{D}$ into the Euler and the continuity equation (Catelan 1995)

$$\boldsymbol{v}[\boldsymbol{x}(\boldsymbol{q}, t), t] = \frac{d}{dt}\boldsymbol{D}(\boldsymbol{q}, t) \quad (13)$$

$$\boldsymbol{g}[\boldsymbol{x}(\boldsymbol{q}, t), t] = \frac{d^2}{dt^2}\boldsymbol{D}(\boldsymbol{q}, t) \quad (14)$$

$$1 + \delta[\boldsymbol{x}(\boldsymbol{q}, t), t] = \det(\mathbf{I} + \mathbf{S})^{-1}\,. \quad (15)$$

formulated in terms of the time variable t. Here, $\mathbf{I}$ is the identity matrix and $\mathbf{S}$ is a 3×3 matrix called the *deformation tensor* with $S_{\alpha\beta} \equiv \partial D_\alpha / \partial q_\beta$ being its elements. If the displacement $\boldsymbol{D}$ is an irrotional field in the Lagrangian space then $S_{\alpha\beta}$ is symmetric. Similarly the Eulerian irrotationality condition $\nabla_{\boldsymbol{x}} \times \boldsymbol{v} = 0$ and the Poisson equation $\nabla_{\boldsymbol{x}} \cdot \boldsymbol{g} = -\alpha(t)\,\delta$ may be written in terms of the displacement after a mathematical effort as (Catelan 1995; Buchert 1993)

$$\epsilon_{\alpha\beta\gamma}\left[(1 + \nabla\cdot\boldsymbol{D})\,\delta_{\beta\sigma} - S_{\beta\sigma} + S^C_{\beta\sigma}\right]\dot{S}_{\gamma\sigma} = 0\,, \quad (16)$$

$$\left[(1 + \nabla\cdot\boldsymbol{D})\,\delta_{\alpha\beta} - S_{\alpha\beta} + S^C_{\alpha\beta}\right]\ddot{S}_{\beta\alpha} = \alpha(t)[J(\boldsymbol{q}, t) - 1]\,, \quad (17)$$

The second equation is the Lagrangian Poisson equation and the first one is the irrotationality condition in Lagrangian space. Both equations dynamically constrain the field $\boldsymbol{D}$. The fundamental question now is how to solve the dynamical equations for the displacements $\boldsymbol{D}$. The irrotationality condition and the Lagrangian Poisson equation are exact equations in the Lagrangian description. It is undoubtedly very difficult to solve them in a rigorous way. A possible alternative is to seek for approximate solutions. The standard technique is to expand the trajectory $\boldsymbol{D}$ in a perturbative series, the leading term being the linear displacement which corresponds

to the Zel'dovich approximation (Buchert 1993; Zel'Dovich 1970). Approximating the Lagrangian Poisson equation implies that the gravitational interaction among the particles of the fluid is described by the first few terms of a Taylor expansion.

$$\boldsymbol{D}(\boldsymbol{q},\tau) = g_1(\tau)\,\boldsymbol{D}^{(1)}(\boldsymbol{q}) + g_2(\tau)\,\boldsymbol{D}^{(2)}(\boldsymbol{q}) + g_3(\tau)\,\boldsymbol{D}^{(3)}(\boldsymbol{q}) + \cdots \quad (18)$$

$\boldsymbol{D}^{(n)}(\boldsymbol{q})$ being the nth-order approximation. The dynamics of the evolution constrains in general both the temporal dependence as described by the functions g_n, and the spatial displacements $\boldsymbol{D}^{(n)}(\boldsymbol{q})$. At any order the solutions are separable in time and space. At first and second orders, the solutions are irrotational in Lagrangian space, i.e. the matrices $D^{(1)}_{a,b}$ and $D^{(2)}_{a,b}$ are symmetric. At the third order it is possible to divide $\boldsymbol{D}^{(3)}$ into three different modes, all separable in space and time. Below are the time functions summarized. They have been used to determine the collapse time of the ellipsoidal collapse (Monaco 1997b):

$$\begin{aligned}
g_1 &= -g(\tau) && (19)\\
g_2 &= -\frac{3}{14} g_1^2 \Omega_m^{-a} && (20)\\
g_{3_a} &= -\frac{1}{9} g_1^3 \Omega_m^{-b} && (21)\\
g_{3_b} &= \frac{5}{42} g_1^3 \Omega_m^{-c} && (22)\\
g_{3_c} &= \frac{1}{14} g_1^3 \Omega_m^{-d} && (23)
\end{aligned}$$

where $g(\tau)$ is given by

$$g(\tau) = 1 + 3\,(\tau^2 - 1)\left[1 + \tau \ln\sqrt{\frac{\tau-1}{\tau+1}}\right]. \quad (24)$$

In order to compute the formation of haloes in Lagrangian perturbation theory one considers the potential of a homogeneous ellipsoid in its principal axis frame, which is given by (Monaco et al. 2002):

$$\psi(\boldsymbol{q}) = \frac{1}{2}(\lambda_1 q_1^2 + \lambda_2 q_2^2 + \lambda_3 q_3^2) \quad (25)$$

where the λ_i are the eigenvalues of the first-order deformation tensor $\boldsymbol{D}^{(1)}_{a,b}(\boldsymbol{q}) \equiv \psi_{,ab}(\boldsymbol{q})$. It is easy now to calculate the perturbative terms from this potential yielding the following local contributions solving all Poisson equations,

$$\begin{aligned}
\psi^{(2)}_{,a} &= \psi_{,a}\psi_{,bb} - \psi_{,ab}\psi_{,b}\\
\psi^{(3a)}_{,a} &= \psi^{C}_{,ab}\psi_{,b} && (26)\\
\psi^{(3b)}_{,a} &= \frac{1}{2}(\psi_{,a}\psi^{(2)}_{,bb} - \psi_{,b}\psi^{(2)}_{,ab} + \psi^{(2)}_{,a}\psi_{,bb} - \psi^{(2)}_{,b}\psi_{,ab})\\
\psi^{(3c)}_{,a} &= \frac{1}{2}(\psi_{,b}\psi^{(2)}_{,ab} - \psi^{(2)}_{,b}\psi_{,ab}).
\end{aligned}$$

With these local contributions one can get the corresponding displacements,

$$\begin{aligned}
D^{(2)}_{a,b} &= \psi_{,ab}\psi_{,cc} - \psi_{,ac}\psi_{,bc}\\
D^{(3a)}_{a,b} &= \psi_{,ac}\psi^{C}_{,bc} && (27)\\
D^{(3b)}_{a,b} &= \frac{1}{2}[D^{(2)}_{ab}\psi_{,cc} - D^{(2)}_{bc}\psi_{,ac} + \psi_{,ab}D^{(2)}_{c,c} - \psi_{,bc}D^{(2)}_{a,c}]\\
D^{(3c)}_{a,b} &= 0.
\end{aligned}$$

Within the Lagrangian perturbation framework the natural definition of collapse is defined as:

$$J(\boldsymbol{q}, g_c) = 0. \quad (28)$$

At this instant the density becomes infinite and different trajectories intersect, forming multi-stream regions. If the Ω_m-dependence of the time functions (19)-(23) is neglected, it is easy to write the condition $J(\boldsymbol{q}, g_c) = 0$ as a third order algebraic equation (Monaco 1995),

$$1 + \lambda_i g_c - \frac{3}{14}\lambda_i(\delta_l - \lambda_i) g_c^2 - \left(\frac{I_3}{126} + \frac{5}{84}\lambda_i\delta_l(\delta_l - \lambda_i)\right) g_c^3 = 0, \quad (29)$$

where it has been used that all the contributions to the deformation tensor are diagonal in the same frame and that the 3c contribution vanishes:

$$\begin{aligned}
\psi_{,11} &= \lambda_1\\
\psi^{(2)}_{,11} &= \lambda_1(\lambda_2 + \lambda_3) && (30)\\
\psi^{(3a)}_{,11} &= \lambda_1\lambda_2\lambda_3\\
\psi^{(3b)}_{,11} &= \lambda_1\lambda_2\lambda_3 + \lambda_1\delta_l(\lambda_2 + \lambda_3)/2
\end{aligned}$$

where $\delta_l = \lambda_1 + \lambda_2 + \lambda_3$. One can already see in the above function how higher order coefficients become increasingly smaller. The next step would be to find the solutions of the above equation order by order.

3.0.1 *First order collapse time*

The first order solution for general ellipsoids is very simple. If only the first term in the Jacobian determinant is taken into account, the definition of collapse gets the simply form

$$\frac{(1+\delta_c)}{(1+\delta_0)} = |\det J^{-1}| = \frac{1+\delta_0}{(1+g^{(1)}\lambda_1)(1+g^{(1)}\lambda_2)(1+g^{(1)}\lambda_3)} \quad (31)$$

The expansion, the shear and the density diverge when

$$1 + g^{(1)}\lambda_3 = 0, \quad (32)$$

where λ_3 is the smallest of the λ_i. Evidently, the first order collapse time is simply given by

$$g_c^{(1)} = -\frac{1}{\lambda_3}. \quad (33)$$

3.0.2 *Second order collapse time*

In the case of second order the Jacobian determinant is given by

$$1 + \lambda_i g_c^{(2)} - \frac{3}{14}\lambda_i(\delta_l - \lambda_i)\left[g_c^{(2)}\right]^2 = 0, \quad (34)$$

and the second order solution for the collapse time results to be (Monaco 1997a)

$$g_c^{(2)} = \frac{7\lambda_3 + \sqrt{7\lambda_3(\lambda_3 + 6\delta_l)}}{3\lambda_3(-\lambda_3 + \delta_l)}\,. \quad (35)$$

It is evident that this solution is limited to $\delta_l \geqslant -\lambda_1/6$. Additionally it should be mentioned that one can differentiate equation (35) with respect to λ_i in order to verify that the 1-axis is the first to collapse.

3.0.3 *Third order collapse time*

For the third order the roots of equation (29) have to be found.

$$1 + \lambda_i g_c - \frac{3}{14}\lambda_i(\delta_l - \lambda_i) g_c^2 + \left(\frac{I_3}{126} + \frac{5}{84}\lambda_i\delta_l(\delta_l - \lambda_i)\right) g_c^3 = 0 \quad (36)$$

This function is a cubic function of the form

$$f(x) = ax^3 + bx^2 + cx + d \quad (37)$$

and can be solved easily with the root-finding formula. After defining new parameters such as

$$q = \frac{3ac - b^2}{9a^2} \qquad r = \frac{9abc - 27a^2d - 2b^3}{54a^3} \tag{38}$$

$$\rho = \sqrt{-q^3} \qquad \theta = \arccos(r/\rho) \tag{39}$$

the solutions for $r^2 > q^3$ are given by

$$x_1 = s + t - \frac{b}{3a}\,, \tag{40}$$

$$x_2 = -\frac{1}{2}(s+t) - \frac{b}{3a} + \frac{\sqrt{3}}{2}(s-t)i\,, \tag{41}$$

$$x_2 = -\frac{1}{2}(s+t) - \frac{b}{3a} - \frac{\sqrt{3}}{2}(s-t)i \tag{42}$$

where s and t are defined as

$$s = (\rho^{\frac{1}{3}}\,, \theta/3) \qquad t = (\rho^{\frac{1}{3}}\,, -\theta/3)\,. \tag{43}$$

Now this general solutions can be applied to the function (29) with the corresponding values for a, b, c and d. Doing so the resulting solution for the third order collapse time has to be chosen as the smallest non-negative one between the following functions (Monaco 1997a)

$$g_{c_1}^{(3)} = -2\sqrt{q}\cos(\theta/3) - (\delta_l/\lambda_i - 1)/14c, \tag{44}$$

$$g_{c_2}^{(3)} = -2\sqrt{q}\cos((\theta + 2\pi)/3) - (\delta_l/\lambda_i - 1)/14c, \tag{45}$$

$$g_{c_3}^{(3)} = -2\sqrt{q}\cos((\theta + 4\pi)/3) - (\delta_l/\lambda_i - 1)/14c, \tag{46}$$

where the following shortcuts have been used

$$c = I_3\lambda_i^3/126 + 5\delta_l/\lambda_i(\delta_l/\lambda_i - 1)/84, \tag{47}$$

$$q = (3(\delta_l/\lambda_i - 1)^2 - 196c)/588c^2. \tag{48}$$

3.1 Lagrangian structure formation

Having carried out the calculation of the collapse time of the ellipsoidal collapse, an analytical expression for the mass function is needed which uses information of the statistical probability distribution function of the initial conditions. This is given by (Doroshkevich 1970):

$$P(\lambda_1, \lambda_2, \lambda_3) = \frac{675\sqrt{5}}{8\pi\sigma^6}\exp\left(-\frac{3}{\sigma^2}r_1^2 + \frac{15}{2\sigma^2}r_2\right)A, \tag{49}$$

where $r_1 = \lambda_1 + \lambda_2 + \lambda_3$, $r_2 = \lambda_1\lambda_2 + \lambda_2\lambda_3 + \lambda_1\lambda_3$, $A = (\lambda_1 - \lambda_2)(\lambda_2 - \lambda_3)(\lambda_1 - \lambda_3)$ and σ^2 given as usual by:

$$\sigma^2 = 4\pi\int\frac{k^2dk}{(2\pi)^3}P(k). \tag{50}$$

Evidently, the probability for two eigenvalues of the deformation tensor to be equal is zero. This means that the isotropic collapse is excluded, implying anisotropical structure formation. It is more convenient to write the probability distribution function as a product of two normalized distributions. For this purpose the following change of variables has to be performed (Monaco 1998)

$$\delta = -\lambda_1 - \lambda_2 - \lambda_3, \tag{51}$$

$$x = \lambda_1 - \lambda_2, \tag{52}$$

$$y = \lambda_2 - \lambda_3. \tag{53}$$

The density contrast δ goes from $-\infty$ to ∞ whereas the other two variables obey the inequalities $x \geqslant 0$ and $y \geqslant 0$, reflecting the original conditions $\lambda_1 \geqslant \lambda_2$ and $\lambda_2 \geqslant \lambda_3$. Carrying out the substitution the probability distribution function becomes

$$P(\delta, x, y) = \frac{1}{\sqrt{2\pi}\sigma}\exp\left(\frac{-\delta^2}{2\sigma^2}\right)\frac{225\sqrt{5}}{4\sqrt{2\pi}\sigma^5}\times \exp\left(-\frac{5(x^2 + xy + y^2)}{2\sigma^2}\right)xy(x+y) \tag{54}$$

One can express the Zel'dovich first order approximation of collapse time in units of the new variables so that equation (33) takes the form

$$g_c^{(1)} = \frac{3}{\delta + x + 2y}. \tag{55}$$

Furthermore, one can define the density contrast needed by a perturbation to collapse at $g_c = 1$ as

$$\delta_c(x, y) = 3 - (x + 2y). \tag{56}$$

In the case of spherical collapse this would reduce to $\delta_c = 3$. It can be seen that the shear lowers the value of δ_c, helping the collapse to occur more easily. With an adequate shear, even underdense perturbations can collapse. As in the case of the Press-Schechter approach, one assumes that a collapsing mass element, whose associated mass is a function of the mass variance σ through the smoothing scale R, $M = M(R(\sigma))$, becomes part of a structure whose mass is greater than M. The mass function is simply the integral of the probability distribution function over all initial conditions (Monaco 1997a,b),

$$F(>M) = \int_0^\infty dx\int_0^\infty dy\int_{\delta_c(x,y)}^\infty d\delta\; P(\delta, x, y), \tag{57}$$

giving the mass function as

$$N(M)dM = -\bar{\rho}\frac{\partial}{\partial M}F(>M)\frac{dM}{M} = -\bar{\rho}\frac{\partial F}{\partial\sigma}\frac{d\sigma}{dM}\frac{dM}{M}. \tag{58}$$

The term $\partial F/\partial\sigma$ contains the dynamical information.

3.2 PINOCCHIO

A compromise between simulations and analytical techniques is a perturbative approach describing the growth of haloes in a given numerical realization of a linear density field, such as the truncated Zel'dovich approximation and the PINOCCHIO algorithm (Taffoni et al. 2002). PINOCCHIO (acronym for *PINpointing Orbit-Crossing Collapsed HIerarchical Objects*) is an algorithm for studying the formation and evolution of dark matter haloes in a given initial linear density field. It was first developed by Monaco et al. (2002). Local parameterisations to the dynamics are used to give precise predictions of the hierarchical formation of dark matter haloes when the correlations in the initial density field are properly taken into account.

This modus operandi enables the automatic generation of a large ensemble of accurate halo merging histories and additionally delivers their spatial distribution. Likewise, the approach can be efficiently applied for generating the input for galaxy formation models since the properties of the halo population are of fundamental importance for understanding galaxy formation and evolution.

PINOCCHIO consists of two steps which determine the hierarchical formation of haloes through accretion and merging:

- The first step handels the definition of the collapse time. Hereby, orbit-crossing will be identified as the instant when a mass element undergoes collapse, without the need to introduce a free parameter. Orbit-crossing is numerically calculated by means of

the ellipsoidal collapse approximation to the full Lagrangian perturbative expansion, as discussed in the previous section (Monaco 1995).

- The second step groups the collapsed particles into disjoint haloes, applying an algorithm similar to that used to identify haloes in n-body simulations.

As explained in the previous subsection, the density diverges as the Jacobian determinant vanishes, corresponding to the formation of a caustic, which states that the transformation $\boldsymbol{x} \rightarrow \boldsymbol{q}$ becomes multi-valued, and particle trajectories undergo orbit crossing. Since the density becomes very high at orbit crossing, it will be identified as the collapse time. In this manner, collapse is very easy to compute using Lagrangian Perturbation Theory which remains valid up to that particular point but breaks down afterwards.

The hierarchical formation of objects is done due to the grouping of orbit-crossing particles into haloes by tracing the merging processes for each particle individually. Briefly, two main processes contribute to the hierarchical clustering: The first one is the accretion of particles onto haloes and the second one the merging of haloes. For this purpose, the particles of the realization are sorted in chronological order of collapse. Starting with the first collapse time the particles are assigned either to a halo or to filaments at the corresponding collapse times. In order for a collapsing particle to accrete on to a halo, it must fulfill a number of conditions. One of them is that the candidate halo must already contain one of its 6 nearest neighbours in the Lagrangian space of initial conditions. The fragmentation process contains 4 different cases which are sufficient for performing the identification and merging history of haloes.

If none of the 6 Lagrangian neighbours have collapsed, then the particle is a local maximum of the inverse collapse time. This particle is a seed for a new halo having the unit mass of the particle and is created at the particle's position. Obviously, the earliest particle to collapse is the first halo.

In the case that the collapsing particle touches only one halo, then the accretion condition, if the halo is close enough, is checked. When the accretion condition is satisfied, then the particle is added to the halo, otherwise it is marked as belonging to a filament. The particles that only touch filaments are marked as filaments as well. If the collapsing particle has more than one touching halo as Lagrangian neighbour, then the merging condition is checked for all halo pairs. Pairs that satisfy the conditions are merged together. The accretion condition for the particle is checked for all touching haloes both before and after merging (when necessary). In the case that the particle can accrete to both haloes, without the haloes merging, it accretes onto that halo for which the distance d in units of halo size R_N is smaller. It may happen that particles fail to accrete even though the haloes merge.

If the collapsing particle does not accrete onto the candidate haloes in the case they are too far, it becomes a filament. But later for this filament particle there is still the possibility to accrete when its neighbour particle accretes onto a halo. This is done in order to mimic the accretion of filaments onto the haloes. Notice that up to 5 filament particles can flow into a halo at each accretion event.

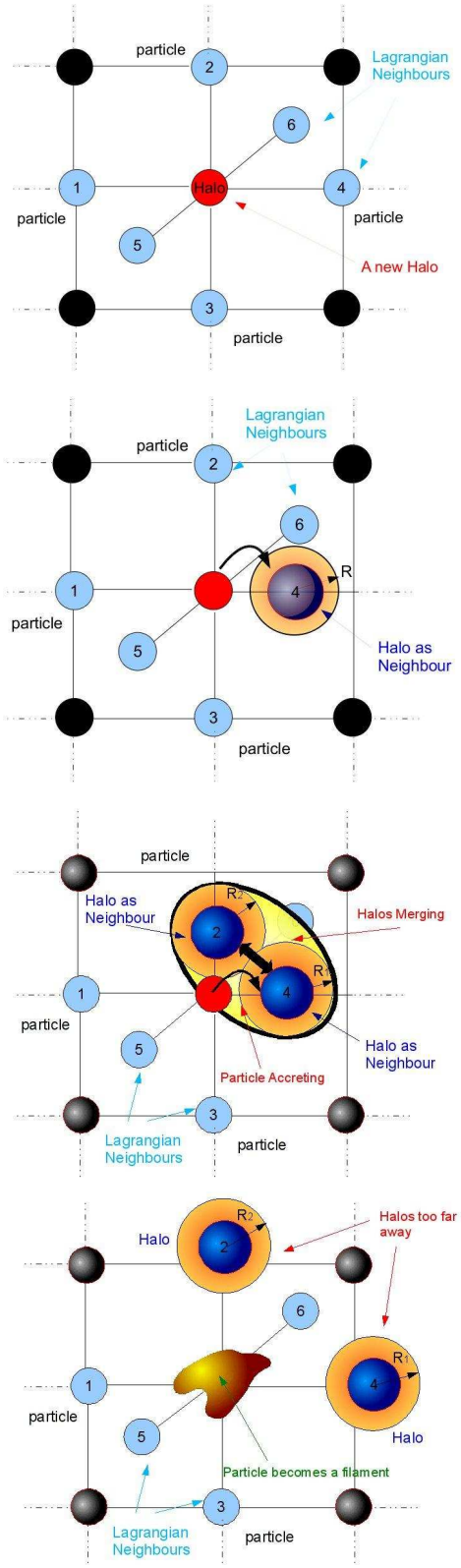

Figure 1. Cases of the fragmentation process: The top panel shows the six Lagrangian neighbours of a given particle, the second panel illustrates how this particle accretes onto a neighbouring halo, the third panel depicts the merging of two haloes and successive accretion and, if there is no accretion, the particle is marked as belonging to a filament in the bottom panel.

3.3 Velocity statistics

In the Eulerian specification of the flow field, the flow quantities are depicted as a function of fixed position $\boldsymbol{q}$ and time t. Specifically, the peculiar velocity is described as:

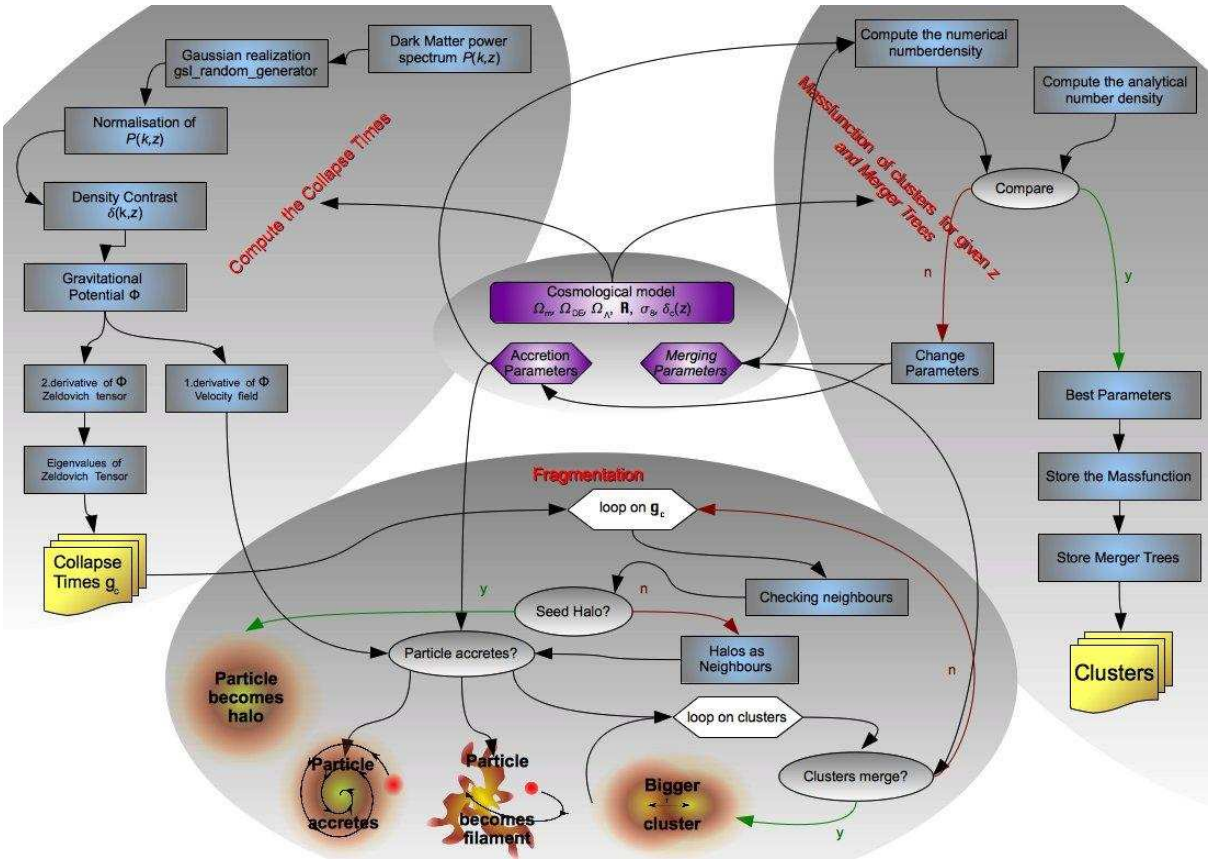

Figure 2. Flow chart of the code: The main 3 blocks of the code are shown. For a given set of parameters (centre) we compute the collapse times (top left) and for each collapsing particle we apply the fragmentation procedure (bottom). Finally we analyse the statistical properties of the fragmented objects (top right).

$$\frac{d}{dt}\boldsymbol{x}(\boldsymbol{q},t) = \frac{\boldsymbol{v}(\boldsymbol{q},t)}{a(t)}. \tag{59}$$

The peculiar velocity expressed in terms of the displacement field $\boldsymbol{D}$ in the Lagrangian specification of the flow field would then be

$$\boldsymbol{v}(t) = \dot{\boldsymbol{x}}(t) = \dot{g}(t)\boldsymbol{D}(\boldsymbol{q}) \tag{60}$$

Now let us study the time evolution of two elements positioned at the Lagrangian coordinates $\boldsymbol{q}_a$ and $\boldsymbol{q}_b$. The Eulerian positions and peculiar velocities at these two points are then given as

$$\boldsymbol{x}_a \equiv \boldsymbol{x}_a(\boldsymbol{q}_a,t) = \boldsymbol{q}_a + g(t)\boldsymbol{D}(\boldsymbol{q}_a) \equiv \boldsymbol{q}_a + g(t)\boldsymbol{D}_a, \tag{61}$$

$$\boldsymbol{x}_b \equiv \boldsymbol{x}_b(\boldsymbol{q}_b,t) = \boldsymbol{q}_b + g(t)\boldsymbol{D}(\boldsymbol{q}_b) \equiv \boldsymbol{q}_b + g(t)\boldsymbol{D}_b, \tag{62}$$

$$\boldsymbol{v}_a(t) \equiv \boldsymbol{v}_a(\boldsymbol{q}_a,t) = \dot{g}(t)\boldsymbol{D}_a, \tag{63}$$

$$\boldsymbol{v}_b(t) \equiv \boldsymbol{v}_b(\boldsymbol{q}_b,t) = \dot{g}(t)\boldsymbol{D}_b, \tag{64}$$

The relative velocity of the two particles is given by

$$\boldsymbol{v}_{ab} = \boldsymbol{v}_b(t) - \boldsymbol{v}_a(t) = \dot{g}(t)(\boldsymbol{D}_b - \boldsymbol{D}_a) \equiv \boldsymbol{v}_\parallel(t) + \boldsymbol{v}_\perp(t), \tag{65}$$

where $\boldsymbol{v}_\parallel(t)$ and $\boldsymbol{v}_\perp(t)$ stands for the components parallel and perpendicular to $\boldsymbol{r}_{ab}(t) \equiv \boldsymbol{x}_b(t) - \boldsymbol{x}_a(t)$. We can now compute the probability distribution function (PDF) of the pairwise peculiar velocity $\boldsymbol{v}$ with separation $\boldsymbol{s}$ from the initial PDF as (Seto & Yokoyama 1998):

$$P(\boldsymbol{v},\boldsymbol{s},t) = \frac{1}{4\pi s^2}\int 4\pi r^2 dr\, dv_{\parallel i} dv_{\perp xi} dv_{\perp yi}\;\; p(v_{\parallel i}, v_{\perp xi}, v_{\perp yi}; r) \times \delta(s - r_{ab}(t))\delta(v - v_{\parallel i}(t)) \tag{66}$$

where $p(v_{\parallel i}, v_{\perp xi}, v_{\perp yi}; r)$ is the initial PDF which depends only on $\boldsymbol{v}_{\parallel i}$ and $\boldsymbol{v}_{\perp i} \equiv \sqrt{v_{\perp xi}^2 + v_{\perp yi}^2}$ where $v_{\perp xi}$ and $v_{\perp yi}$ are the two components of $\boldsymbol{v}_{\perp i}$ perpendicular to each other. i denotes quantities at some initial time.

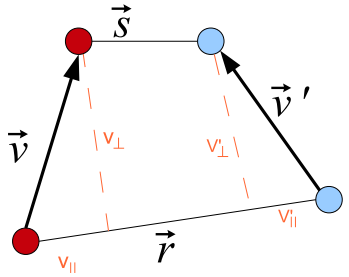

Figure 3. the visualisation of the configuration

Putting the Eulerian positions and peculiar velocities in the above PDF gives:

$$P(\boldsymbol{v},\boldsymbol{s},t) \propto \int_{r^\star}^{\infty} r dr\;\; p(v^\star_{\parallel i}, v^\star_{\perp i}; r), \tag{67}$$

where $v^\star_{\parallel i}$ and $v^\star_{\perp i}$ stand for

$$v^\star_{\parallel i} \equiv \frac{\dot{g}_i}{g}\left(\frac{s^2}{r} - \frac{sg}{r\dot{g}}v - r\right), \tag{68}$$

$$v^\star_{\perp i} \equiv \frac{\dot{g}_i}{g}s\left(1 - \frac{s^2}{r^2} - \frac{g^2}{r^2\dot{g}^2}v^2 + \frac{sg}{r^2\dot{g}}v\right), \tag{69}$$

$$r^\star \equiv \left|s - \frac{g}{\dot{g}}v\right|. \tag{70}$$

We have to specify the initial PDF $p(\upsilon^\star_{\|i}, \upsilon^\star_{\perp i}; r)$ in order to be able to compute the desired PDF $P(\boldsymbol{\upsilon}, \boldsymbol{s}, t)$. As we were dealing with the longitudinal mode, the peculiar velocity in the linear regime is related to the $\delta(\boldsymbol{x}, t)$ and accordingly to its Fourier transform $\delta_{\boldsymbol{k}}(t)$

$$\boldsymbol{\upsilon}(\boldsymbol{x}, t) = i\frac{\dot{g}_i}{g_i}\int \frac{\boldsymbol{k}}{k^2}\delta_{\boldsymbol{k}}(t_i)e^{i\boldsymbol{kx}}\frac{d^3k}{(2\pi)^3}. \quad (71)$$

It is important to emphasize that the initial pairwise peculiar velocities are Gaussian distributed like the initial density fluctuations. From the velocity correlation tensor $\left\langle \upsilon_i \upsilon_j \right\rangle$ one obtains the projections:

$$\langle \upsilon_\| \upsilon_\| \rangle = \sum_{i,j}\left(r_i^\| r_j^\| - \frac{1}{3}\delta_{ij}\right)\left\langle \upsilon_i \upsilon_j \right\rangle, \quad (72)$$

$$\langle \upsilon_\perp \upsilon_\perp \rangle = \sum_{i,j}\left(r_i^\perp r_j^\perp - \frac{1}{3}\delta_{ij}\right)\left\langle \upsilon_i \upsilon_j \right\rangle. \quad (73)$$

Thus, the two-point correlation functions are given by (Gorski 1988):

$$\langle \upsilon_{\|i} \upsilon_{\|i} \rangle = \frac{1}{6\pi^2}\left(\frac{\dot{g}_i}{g_i}\right)^2 \int dk P_i(k)\left(1 - 3j_0(kr) + 6\frac{j_1(kr)}{kr}\right) \quad (74)$$

$$\langle \upsilon_{\perp i} \upsilon_{\perp i} \rangle = \frac{1}{6\pi^2}\left(\frac{\dot{g}_i}{g_i}\right)^2 \int dk P_i(k)\left(1 - 3\frac{j_1(kr)}{kr}\right) \quad (75)$$

Finally, the initial probability distribution function is given by

$$p(\upsilon^\star_{\|i}, \upsilon^\star_{\perp i}; r) = \frac{e^{-T}}{\sqrt{(2\pi)^3 Y_\|(r) Y_\perp^2(r)}}, \qquad T \equiv \frac{(\upsilon^\star_{\|i})^2}{2Y_\|(r)} + \frac{(\upsilon^\star_{\perp i})^2}{2Y_\perp(r)} \quad (76)$$

where $\langle \upsilon_{\|i} \upsilon_{\|i} \rangle \equiv Y_\|(r)$ and $\langle \upsilon_{\perp i} \upsilon_{\perp i} \rangle \equiv Y_\perp(r)$. Therefore, we can now obtain the desired PDF $P(\boldsymbol{\upsilon}, \boldsymbol{s}, t)$ through the integration $P(\boldsymbol{\upsilon}, \boldsymbol{s}, t) \propto \int_{r^\star}^\infty r dr \;\; p(\upsilon^\star_{\|i}, \upsilon^\star_{\perp i}; r)$. We relate the distance $\boldsymbol{r}$ in the analytical model to the distance of two haloes at the time of merging. Furthermore we substitute for the power spectrum a filtered spectrum smoothed at a wavelength which corresponds to the halo mass. Computing the velocity distribution at a distance $\boldsymbol{s}$ corresponding to the merging condition yields distributions very similar to the ones obtained by PINOCCHIO. In particular we confirm the trend of steeper distributions at lower mass ratio.

As expected the velocity distribution for the analytical PDF is shallower than the distribution from PINOCCHIO data. This reflects the fact that merging processes in PINOCCHIO conserve momentum but not energy since merging is an inelastic collision. At each merging the velocity of the final halo is given by $\upsilon_f = \upsilon_1 m_1 + \upsilon_2 m_2/(m_1 + m_2)$ since the momentum is conserved. Because of the energy loss high velocities do not appear in the PINOCCHIO velocity distribution and therefore the curve decreases faster. But the loss of energy does not occur in the analytical configuration and therefore the curve is shallower.

4 RESULTS

In the following we present the results from a simulation for 64^3 particles in a box of side length 128 Mpc/h, carried out in the framework of Lagrangian perturbation theory with our C++ reimplementation of the PINOCCHIO code for following the merging activity of the large-scale structure.

The first step was to create a realisation of a Gaussian density field for a specified ΛCDM spectrum. From the density contrast the gravitational potential and Zel'dovich tensor were derived. Differentiations were performed again in Fourier space allowing us to recover the quantities with minimum noise. For each point $\mathbf{q}$ of the Lagrangian initial coordinates and each smoothing radius R, the collapse time, determined by the time at which the particle is predicted to enter a high-density multi-stream region, and ellipsoidal truncation were then computed using Lagrangian perturbation theory. Determining the eigenvalues of the Zel'dovich tensor, it is straightforward to calculate the collapse times evaluating the expressions of the individual orders (46). For each particle only the earliest collapse time is recorded with the corresponding smoothing radius and velocity. The third order Lagrangian prescription improves the collapse times. The particles collapse earlier and thus the merging process starts sooner. The first axis to collapse is the one corresponding to the smallest λ_3 eigenvalue indicating the convergence and the fact that the Zel'dovich approximation makes the largest contribution to collapse dynamics. The collapsed medium is then fragmented into isolated objects using the algorithm which we described above to mimic the accretion and merger events of hierarchical collapse. We distinguish between collapsed particles belonging to relaxed haloes or to lower-density filaments using the accretion and merging conditions. Directly after the fragmentation process was completed we studied the relative velocities of the haloes by merging.

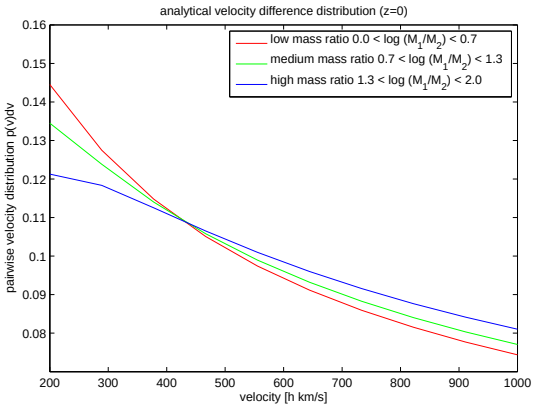

Figure 4. The analytical pair velocity probability density for three intervals in mass ratio: low mass ratio $0.0 < \log(M_1/M_2) < 0.7$ (red line), medium mass ratio $0.7 < \log(M_1/M_2) < 1.3$ (green line) and high mass ratio $1.3 < \log(M_1/M_2) < 2.0$ (blue line).

Figs. 5 and 6 illustrate structure formation dynamics in the Lagrangian picture: Matter is transported out of initially underdense regions and is accumulated in superstructures, where merging is prominent due to the high particle density. In fact, the most massive objects are found in regions of converging velocities, a nice example of which can be found in the upper right front corner of the simulation cube. One sees coherent flow patterns on the scale of the correlation length of the density field. In the vicinity of massive structures one can observe larger relative velocities compared to underdense regions. This can be traced back to the fact that the velocity field of an overdense region has a larger variance compared to the cosmological average. The statistics of the velocity field is translated to that of the haloes by imposing momentum conservation in the merging process. Therefore, the figure confirms the expectation of high pairwise velocities in overdense regions.

In order to compare our results with the milliMillennium Simulation (Springel et al. 2005) we have applied the same merging conditions to the milliMillennium data. In Figures 7 - 12 we compare the probability distribution of the relative velocity at the ti-

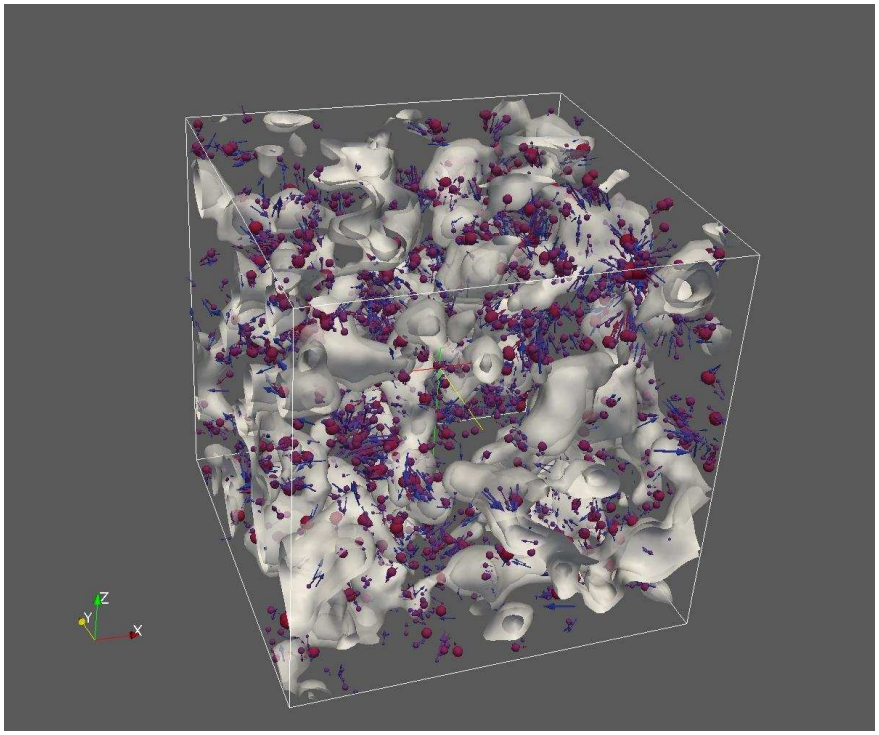

Figure 5. Density field, smoothed with a Gaussian kernel of 8 Mpc/h, with contours at -2σ and -3σ, superimposed on the velocity field visualised by arrows and the halo distribution, where the size of the spheres is indicative of the logarithmic halo mass. The side length of the cube corresponds to 128 Mpc/h.

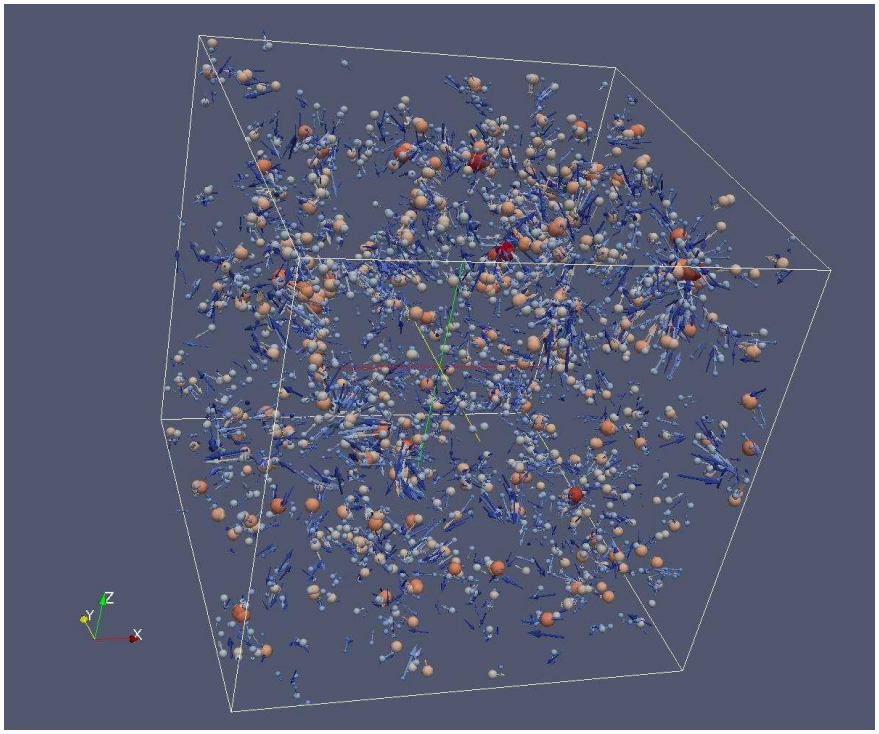

Figure 6. Similar to Fig. 5 only without isodensity contours for making the velocity field more visible. Logarithmic halo mass is indicated by colour and size, and the arrow length is proportional to the halo velocity.

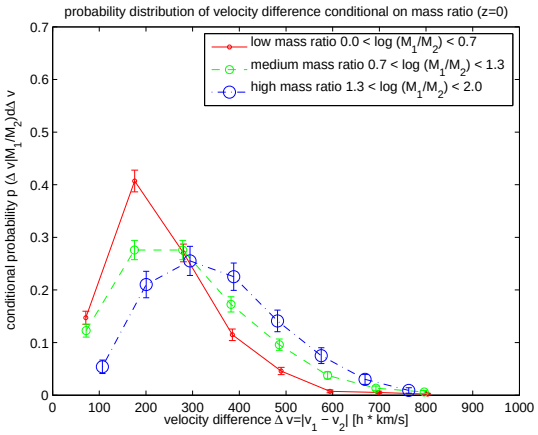

Figure 7. probability distribution of velocities conditional on the halo mass ratio for redshift $z = 0$ from our simulation

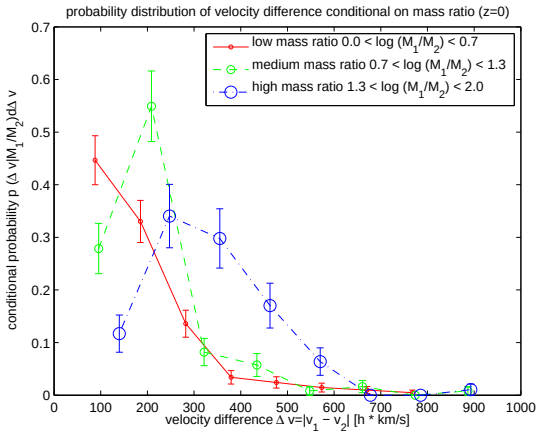

Figure 10. probability distribution of velocities conditional on the halo mass ratio for redshift $z = 0$ from the milliMillennium simulation

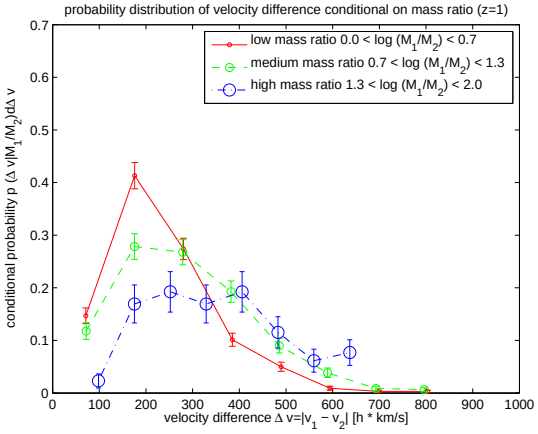

Figure 8. probability distribution of velocities conditional on the halo mass ratio for redshift $z = 1$ from our simulation

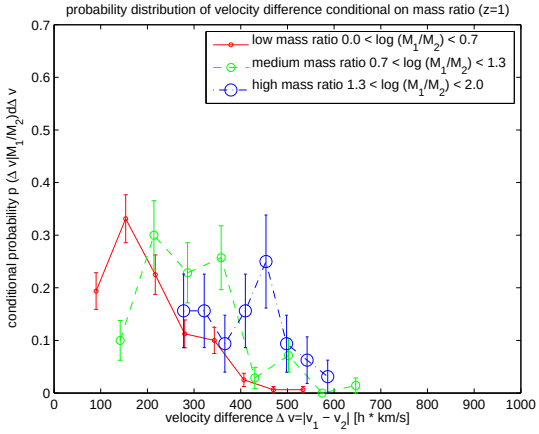

Figure 11. probability distribution of velocities conditional on the halo mass ratio for redshift $z = 1$ from the milliMillennium simulation

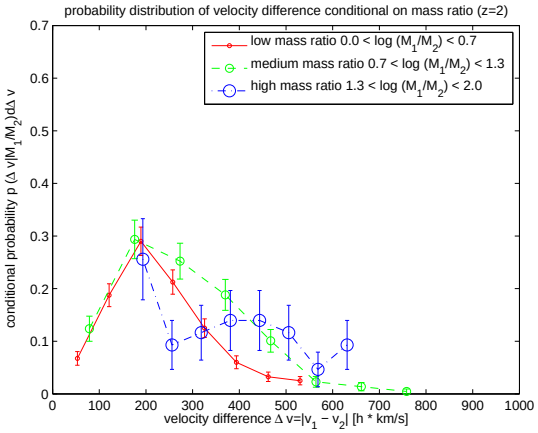

Figure 9. probability distribution of velocities conditional on the halo mass ratio for redshift $z = 2$ from our simulation

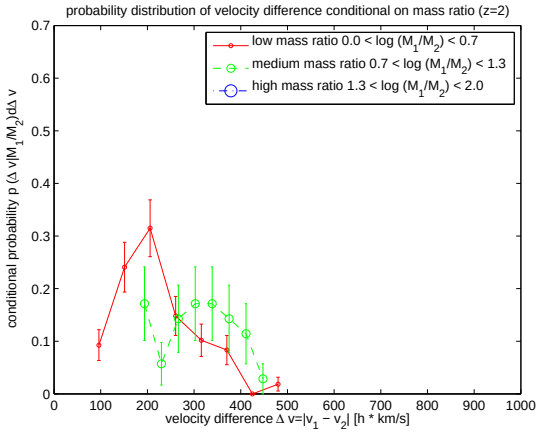

Figure 12. probability distribution of velocities conditional on the halo mass ratio for redshift $z = 2$ from the milliMillennium simulation

me of merging, for three different mass ratio intervals: approximately equal masses $\log(M_1/M_2) < 0.7$, intermediate values for the mass ratio $0.7 < \log(M_1/M_2) < 1.3$ and high mass ratios $\log(M_1/M_2) > 1.3$. The data is further split into three redshifts: $z = 0, 1, 2$, where at $z = 2$ the numbers of massive haloes is not sufficient for deriving the probability density as statistical error bars are too large to draw conclusions. We subdivide the velocity range between the smallest and largest velocity into 10 bins which allows us to investigate the features of the velocity distribution while obtaining reasonable statistical error bars, and normalise all histograms to unity. The statistics of milliMillennium-data are slightly worse due to a smaller volume ($V = (62.5\ \mathrm{Mpc/h})^3$, $N = 270^3$) compared to the PINOCCHIO runs ($V = (128\ \mathrm{Mpc/h})^3$, $N = 64^3$).

Quite generally, the figures reproduce the basic behaviour expected from analytical arguments as outlined in Sect. 3.3. The distributions are steeper at lower mass ratio in both the Millennium data set as well as in PINOCCHIO. The shape of the distributions between PINOCCHIO and the Millennium simulation is very similar, in particular at low redshifts, with the curves for the intermediate and the high mass ratio peaking at almost identical values for the relative velocity. All curves terminate at velocities of $\simeq 700$km/s underlining the sparcity of high-velocity mergings (Hayashi & White 2006) and the small simulational volumes. Naturally we expect the distributions of the milliMillennium simulation to drop faster than corresponding distributions from PINOCCHIO because the latter treats merging processes as an inelastic collision and does not follow the dissipative dynamics inside haloes.

5 SUMMARY

The aim of this paper is an investigation of merging processes in the cosmic large-scale structure in the framework of Lagrangian perturbation theory and to compare the results for the pairwise velocity distribution obtained with an adaptation of the PINOCCHIO algorithm to *n*-body data.

- It is comparatively simple in PINOCCHIO to construct merger trees as it is not necessary to identify haloes in the particle distribution and as one can directly follow the merging processes between haloes, such that the haloes in PINOCCHIO correspond to friends-of-friends particle groups in *n*-body simulations.
- Halo properties, such as the distribution of masses, spins and now also merger trees and pairwise velocities can be reliably derived from a Lagrangian code, with the differences in the distribution being smaller than the statistical error bars. Hereby, we have investigated the derivation of the mass function from PINOCCHIO, optimised the parameter choices for providing a better agreement with analytical functions compared to the numbers quoted by Monaco et al. (2002) and used these parameters for our studies of the velocity distributions. We have also investigated that the velocities show the correct scaling with cosmological parameters, and the correct scaling with halo mass ratio in comparison to an analytical calculation.
- In comparison to an analytical pairwise velocity distribution, PINOCCHIO is able to reproduce the trend of shallower distributions with increasing halo mass ratio. At high velocities, however, PINOCCHIO exhibits a steeper behaviour compared to that predicted by the analytical calculation at fixed mass ratio, which is explained by the fact that merging processes in PINOCCHIO are treated as inelastic collisions with conserved momentum but not conserved energy. Because of this energy loss, high velocities are not present in PINOCCHIO data and the distribution is steeper.
- We find a general agreement between the velocity distributions of PINOCCHIO and the milliMillennium simulation, both in terms of relative numbers and values for the absolute velocity. Additionally, the scaling with redshift and mass ratio between merging haloes behaves very similarly. The peaks of the distributions at low redshifts coincide with each other, and although distributions from the milliMillennium simulation terminate earlier, this feature is not unexpected as PINOCCHIO does not treat the dissipative dynamics of merging haloes. Again, the correct dependence of pairwise velocity with halo mass ratio is recovered.
- PINOCCHIO, relying on a phenomenological description of the merging process of two haloes and combining the individual momenta in an inelastic collision is very fast compared to *n*-body codes, which allows sweeps in the parameter space relevant to peculiar velocities, i.e. Ω_m, σ_8 and the dark energy parameters, for which we have verified the basic relations expected by linear structure formation.

Further questions include the environment-dependence of velocity statistics, which is comparatively easy to do in Lagrangian perturbation theory. A very useful discriminant for this purpose is the number of positive eigenvalues of the shear tensor. One would expect smaller velocities inside voids and larger velocities in supercluster regions. In fact, this dependence can already be seen in Fig. 5. Other extensions include the investigation of two-point statistics of the velocity field, and to answer questions related to velocity statistics (Regos & Szalay 1995). Anaglyphic versions of Figs. 5 and 6 are available on request from the authors.

ACKNOWLEDGEMENTS

We thank Volker Springel for his suggestions and access to the Millennium data base. LH's work is partially funded by the SNF. BMS's work is supported by the Graduate School of Fundamental Physics in the framework of the DFG's Excellence Initiative. We would like to thank Pierluigi Monaco for his help concerning PINOCCHIO's parameter choices, Francesco Pace for answering questions on the original FORTRAN code and Jean-Claude Waizmann for his suggestions to improve the figures.

Literatur

Bardeen J. M., Bond J. R., Kaiser N., Szalay A. S., 1986, ApJ, 304, 15
Bernardeau F., Colombi S., Gaztañaga E., Scoccimarro R., 2002, Physics Reports, 367, 1
Buchert T., 1992, MNRAS, 254, 729
Buchert T., 1993, in G. Börner & T. Buchert ed., High Energy Astrophysics and Cosmology Higher-order Lagrangian perturbation theory. pp 204–214
Buchert T., 1996, in S. Bonometto, J. R. Primack, & A. Provenzale ed., Dark Matter in the Universe Lagrangian Perturbation Approach to the Formation of Large-scale Structure. pp 543–564
Buchert T., Weiss A. G., 1993, in F. Bouchet & M. Lachieze-Rey ed., Cosmic Velocity Fields Third-order Lagrangian perturbation theory - realization at high-spatial resolution. pp 517–+
Catelan P., 1995, MNRAS, 276, 115
Doroshkevich A. G., 1970, Astrophysics, 6, 320
Gorski K., 1988, ApJL, 332, L7
Hayashi E., White S. D. M., 2006, MNRAS, 370, L38
Monaco P., 1995, ApJ, 447, 23

Monaco P., 1997a, MNRAS, 287, 753
Monaco P., 1997b, MNRAS, 290, 439
Monaco P., 1998, Fundamentals of Cosmic Physics, 19, 157
Monaco P., Theuns T., Taffoni G., 2002, MNRAS, 331, 587
Regos E., Szalay A. S., 1995, MNRAS, 272, 447
Sahni V., Coles P., 1995, Physics Reports, 262, 1
Seto N., Yokoyama J., 1998, ApJ, 492, 421
Springel V., White S. D. M., Jenkins A., Frenk C. S., Yoshida N., Gao L., Navarro J., Thacker R., Croton D., Helly J., Peacock J. A., Cole S., Thomas P., Couchman H., Evrard A., Colberg J., Pearce F., 2005, Nature, 435, 629
Sugiyama N., 1995, ApJS, 100, 281
Taffoni G., Monaco P., Theuns T., 2002, MNRAS, 333, 623
Zel'Dovich Y. B., 1970, A&A, 5, 84

This paper has been typeset from a TEX/ LATEX file prepared by the author.